Heliyon 10 (2024) e34481

Contents lists available at ScienceDirect

Heliyon

journal homepage: www.cell.com/heliyon

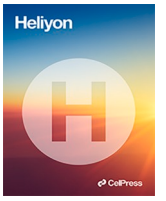

Research article

Numerical investigation on the impact of different design arrangements of helical heat exchangers with varying cross-sections utilizing ternary hybrid nanofluids

Mostafa Kamal Fahad [a], Md. Jahid Hasan [b,*], Nowroze Farhan Ifraj [a], Dipta Chandra Dey [a]

[a] Department of Mechanical and Production Engineering (MPE), Ahsanullah University of Science and Technology, Dhaka-1208, Bangladesh
[b] Department of Mechanical and Production Engineering (MPE), Islamic University of Technology (IUT), Board Bazar, Gazipur, 1704, Bangladesh

ARTICLE INFO

Keywords:
Helical heat exchanger
Nusselt number
Entropy generation
Ternary hybrid nanofluid
MCDM

ABSTRACT

Helical tube heat exchangers (HTHE) are commonly used as thermal devices in various thermal engineering applications. A comparative investigation was undertaken to examine several helical tube designs in relation to their potential uses with water and nanofluids. Additionally, employing the ternary hybrid nanofluid (THNF) flow in helical-type heat exchangers to assess the heat transfer and frictional loss is a unique concept, as there is currently no research on this specific application. This study involves analyzing three different design configurations, each of which has three different inlet profiles: round, square, and oval shapes. Hence, a numerical analysis has been conducted on nine cases, each including the same pipe length, helix diameter, and pitch distance. The specified range for the Reynolds number under the water and THNF flow condition is 5000–25000. The results are acquired for both fluids, considering the Nusselt number (Nu), friction factor (f), outlet temperature (T_{out}), and entropy production (S_g). Multi-Criteria Decision Making (MCDM) is employed to provide a thorough assessment of the overall performance of the proposed designs. The results have been shown as graphical representations, streamlines and contours where Nusselt number, friction factor and entropy generation have been evaluated. The Nusselt number has a higher value for the oval cross-section, while it reaches its lowest value for the square cross-section. The highest heat transfer rate is got for Design 1 with the oval-shaped case. The friction factor for a circular cross-section HHTE is 48 % higher than the friction factor for a square cross-section profile. In addition, the square shape at a Reynolds number (Re) of 25000 exhibits 5 % less entropy formation compared to the oval shape geometry at a Reynolds number of 5000. The results of MCDM analysis indicate that Design 1, which features a square section, exhibits superior performance. Conversely, Design 2, which incorporates a circular cross-section, demonstrates poor performance. Among the six ternary hybrid nanofluids, the Al_2O_3+CNT+Graphene nanofluid with a water basis exhibits the greatest Nusselt number.

Nomenclature

Symbols *Abbreviation*

(*continued on next page*)

* Corresponding author.
E-mail address: jahidhasan@iut-dhaka.edu (Md.J. Hasan).

https://doi.org/10.1016/j.heliyon.2024.e34481
Received 1 April 2024; Received in revised form 10 June 2024; Accepted 10 July 2024
Available online 11 July 2024

(*continued*)

A_c	Area of cross section (m^2)	RANS	Reynolds averaged navier-stokes
A_s	Surface area of pipe (m^2)	DSTHE	Double spiral tube heat exchanger
C_p	Specific heat (J/Kg-K)	HCTT	Helical coiled trilobal tube
P	Pitch length (m)	CNT	Carbon nanotube
S_g	Entropy generation ($JKg^{-1}K^{-1}$)	SHCTHE	Shell and helical coil tube heat exchanger
D_h	Hydraulic diameter (m)	HCTHE	Helical coil tube heat exchanger
d_h	Helix diameter (m)	HTHE	Helical tube heat exchanger
Re	Reynolds number	MCDM	Multi-criteria decision making
E_{ij}	Rate of Deformation	THNF	Ternary hybrid nanofluid
f	Friction factor	TSTHE	Triple spiral tube heat exchanger
h	Surface heat transfer coefficient (W/m^2-K)	LMTD	Log mean temperature difference
T_{in}	Inlet temperature (K)	*Greek Symbols*	
T_o	Outlet temperature (K)		
V	Inlet velocity (m/s)	ρ	Density (Kg/m^3)
L	Pipe length (m)	μ	Dynamic viscosity (Kg/m-s)
L_1	Helix length (m)	ϕ	Volume fraction of nanofluid
T_w	Wall temperature (K)	μ_t	Eddie viscosity
d_i	Diameter of inner helix (m)	ε	Turbulence dissipation rate (m^3s^{-2})
d_o	Diameter of outer helix (m)	*Subscripts*	
N	Number of turns	*np*	Nanoparticle
$\dot{m}$	Mass flow rate (Kg/m^3)	*hnf*	Hybrid nanofluid
k	Thermal conductivity (W/m-K)	*BF*	Base fluid
Nu	Nusselt number	*nf*	Nanofluid
q_{wall}	Heat flux at pipe wall (W/m^2)	*thnf*	Ternary hybrid nanofluid
Δp	Pressure difference (Pa)		

1. Introduction

Heat exchangers are apparatuses designed to aid in transferring heat energy between diverse fluid mediums. They significantly impact thermal exchange in various applications, including power generation, temperature regulation, electronic devices, pharmaceuticals, automotive equipment, and more [1–4]. Additionally, there's a growing interest in enhancing the outputs of these thermal devices as part of efforts to augment efficiency in thermal energy systems [5–10]. Helical tube heat exchangers (HTHE) attracted considerable attention for their unique attributes that increase heat transmission, making them stand out from other heat exchangers. In the context of an HTHE, fluid flow generates a secondary flow due to an axial pressure differential along with the primary fluid flow. Fluid flow in an HTHE changes from linear to curved streams as it transitions from straight to coiled paths. This alteration in the rhythm of fluid motion leads to higher momentum and heat transfer rates [11].

Based on existing reports, it has been shown before that HTHE outperforms traditional straight-type tube heat exchangers [12]. Kurnia et al. [13] assessed the efficiency of boosting heat transmission and entropy production for low Reynolds numbers through coiled pipes of various sectional forms compared to plain tubes with identical segments. Results suggest that coiled tubes have a higher heat transmission rate. Furthermore, a decrease in entropy production was observed, indicating its efficiency compared to straight pipes. Maghrabie et al. [14] evaluated the thermic transfer along with the pressure differential characteristics of a shell and helical coil tube heat exchanger (SHCTHE), leveraging different tilt angles and Dean numbers (De). The results indicate SHCTHE's effectiveness vertically is more than horizontally, with a respective increase of 26.3 % and 23.1 % for De 1540 and 3860. Wang et al. [15] performed CFD analysis of the shell part of a helical coiled trilobal tube (HCTT). It was concluded that the fluid on the shell part of the HCTT has a major capacity to induce rotation and disrupt boundary layers. The velocity leveling around the tubular wall shows an increase in both the circumferential and radial directions and the velocity vectors correlate well with the temperature difference. Narrein and Mohammed [16] investigated the impacts of four different nanofluids on a helically coiled tube heat exchanger (HCTHE). In this work, the use of a nanofluid containing dispersed CuO particles in water allows the Nusselt number (*Nu*) to achieve its maximum value. Mahmoud Abdelmagied [17] introduced an innovative configuration for a heat exchanger noted as a triple spiral tube heat exchanger (TSTHE) and conducted a comparative analysis in conjunction with a pre-existing double spiral tube heat exchanger (DSTHE). As per the findings, when subjected to identical flow conditions, the *Nu* derived from a TSTHE was greater as opposed to a DSTHE. The outcomes suggested that although the increase in pressure gradient is negligible, the hot fluid input's temperature significantly influences the *Nu*. Naphon et al. [18] used computational methods to examine the fluid-flow characteristics and thermal-hydraulic effects of coiled tubes of spiral shape, both with and without helical ribs. Tubes having ribs, which are spirally coiled, have a *Nu* that is 12.45 % higher than the tube without ribs. However, the drop of pressure across the analyzed section increases due to the complexity and roughness of the flow.

Recently, numerous innovative design concepts have been suggested to compare them in terms of effective performance for various applications. Javadi et al. [19] introduced several new helical ground heat exchangers and evaluated their effectiveness compared to a single U-type spiral tube heat exchanger. The findings illustrate that the triple helix had better thermal performance, succeeded by the double helix and W-type helix. Marzouk et al. [20] developed six distinct arrangements of multi-HTHE with different surface areas. Reddy et al. [21] included a copper tube in a HTHE setup. By implementing this modification, they achieved as much as 17.05 % augmentation for *Nu* and found a 15 % improvement in the *f*. Noorbakhsh et al. [22] investigated the exterior and internal coil diameter and internal and external coil pitch in their study. Based on their findings, a pitch of 50 mm showed the highest thermal

efficacy for internal coils, while a pitch of 60 mm was shown to be the most effective for external coils. Lu et al. [23] investigated the thermal effects of a shell and triple helical coil heat exchanger. This study employed empirical and computational methods simultaneously to assess the flow at high *Re*. The *Nu* of the shell part was calculated using the Wilson diagram. To improve the solidifying nature of an ice storage system, Pakjad et al. [24] made use of a newly developed serpentine-tube heat exchanger. The characteristics they examined were the diameter of the tube and the distance between winding rows. According to their findings, widening the distance between zigzag tube rows leads to a higher ice accumulation on the structure. More precisely, the rate at which ice is formed increases by 24.68 % when the space between serpentine tube rows is at its largest, compared to instances where the gap is at its minimum.

Although helical tube heat exchangers have been extensively studied, with research focusing on the alteration of surfaces [25,26], variation of inlet profiles [27], optimization of curvature parameters [28,29] and the use of conventional fluids are found to be inefficient in terms of overall heat transmission, primarily for their lower thermal-conductivity. Therefore, the adoption of nanofluids has gained significant interest throughout the years. A nanofluid is a mixture of nanoparticles evenly dispersed within various familiar liquids. Nanoparticles incorporated in base fluids generally have dimensions not exceeding 100 nm. Nanofluids have the potential to achieve higher energy efficiency compared to their base fluids because of enhanced heat capacity, combined impacts of tiny particles, Brownian motion of small particles and the decrease in the height of the boundary layer [30]. Significant research is currently being conducted on nanofluids, exploring various combinations of volume fractions. Elsaid et al. [31] conducted experiments with nanofluids consisting of Al_2O_3-water, MgO-water, and TiO_2-water. These experiments are conducted using shell-and-tube heat exchangers having cross sections of different shapes. Their findings indicate that the round segment yielded the highest *Nu*, with a significant increase of 62.5 %. Mahmoudi et al. [32] examined heat transfer and frictional effects in helically coiled pipes with TiO_2/water as the operating fluid. In their study, Elsaid et al. [33] examined hybrid nanofluids comprehensively, examining their thermal, frictional, and exergy properties. The study focused on four specific types of nanoparticles: Al_2O_3, MgO, SiC, and MWCNT. Yarmand et al. [34] synthesized GNP–Ag/water hybrid nanofluids in a tubular pipe under constant flux of heat. Bouselsal et al. [35] conducted research on shell and tube heat exchangers by altering the tube shape and investigating the effect of Al_2O_3-MWCNT hybrid nanofluid effect on the entropy generation and heat transfer rate.

After years of research, it has been established that both single and hybrid nanofluids exhibit remarkable heat transfer properties [36–38]. Nevertheless, enhancing their characteristics involves modifying the percentage of nanoparticles, which leads to an enhancement in fluid resistance. To address these challenges, scientists created functional fluids by combining three nanoparticles with a conventional fluid called a 'ternary hybrid nanofluid' (THNF) [39]. Alawi et al. [40] conducted experiments utilizing mono, hybrid, and ternary-nanofluids in a pipe equipped with turbulators. Arif et al. [41] developed a model to study the heat transmission of radiators using ternary nanofluids based on water. Sahoo [42] conducted a study on the thermic examination of a radiator utilizing three different nanoparticles. The outcomes showcased an enhancement of 18.3 % in thermal transport and 6.3 % in second law efficacy when the volume concentration of these materials was between 1 and 3%. Fetuga et al. [43] suggested using torus, stent, and surface-grooved twisted tape to enhance heat transfer in a pulsing heating condition. They achieved this by utilizing different concentrations of ternary nanofluids, including SiO_2, ZnO, and CaO nanoparticles. Kumar and Sahoo [44] examined the characteristics of

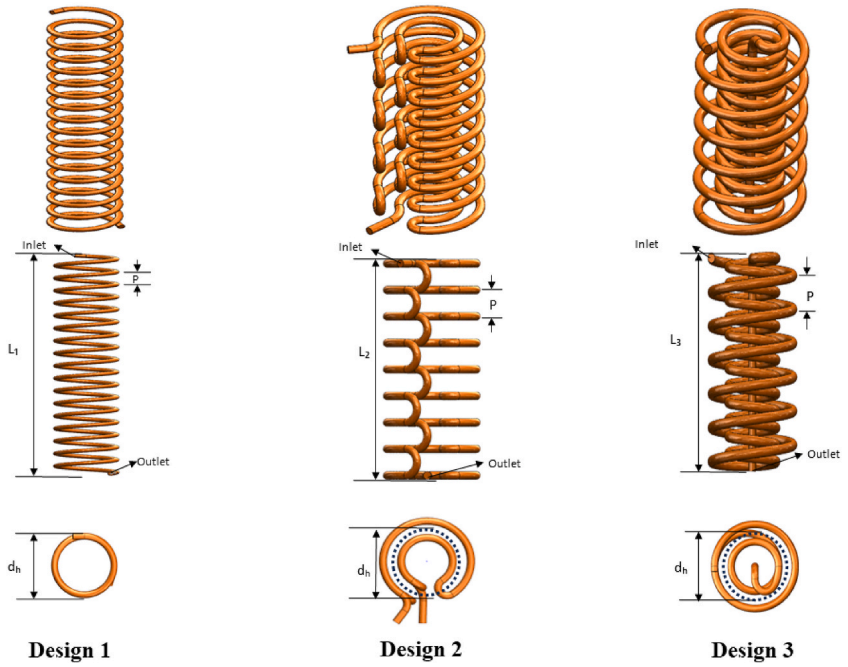

Fig. 1. Three different designs of helical-type heat exchangers.

an air-heater-eat-exchanger with various inserts. They utilized ternary nanofluids, including Al_2O_3, graphene, and CNT nanoplatelets. Berrehal et al. [45] proposed mass-based model for the hybrid nanofluid as a novel model and tested for a wedge with a relative motion. Dharmaiah et al. [46] conducted numerical analysis on a wavy cylindrical object using nanofluid and developed a model for energy activation.

Since HTHE is mostly used in thermal engineering applications such as power generation, geothermal applications, chemical industries, etc., the device's thermal performance is the most significant concern for engineers. In the studies relating to HTHE, their innovative design plays the most crucial role in enhancing heat transmission by creating secondary flows which promotes greater fluid mixing and energy redistribution. However, the formation of such fluid flow results in higher pumping power which decreases the efficiency of this mechanical device. Therefore, to achieve greater efficient design, comparison among different design configurations of HTHE is needed which are studied by several research attempts [19,20,47,48]. Moreover, varying the cross section can lead to improved flow dynamics and various pressure drops [4,13,27]. But, to the best of the author's knowledge, no study has been conducted on the comparison of innovative helix designs with the alteration of inlet profiles. Additionally, the authors are aware of no literature describing the use of ternary hybrid nanofluids in HTHE devices. Therefore, the current study gives a comparative analysis of three distinct HTHE designs with three inlet profiles, namely circular, oval, and square, with equal pipe length, pitch and helix radius. The main goal is to determine the best design configuration and evaluate the effect of helix design variation, different inlet profiles and the application of ternary hybrid nanofluid on the overall performance. To evaluate the effectiveness of the initial instances, the Multi Criteria Decision Making (MCDM) approach has been used. After the initial diagnosis of these models with water, ternary nanofluids have been applied with the best design.

2. Description of the problem

2.1. Definition of fluid domain and classification of geometric type

This current study demonstrates various unique design arrangements of helix-type tube heat exchangers in Fig. 1. With the aid of complex intricate design, this type of heat exchanger shows enhanced thermal energy exchange. A wide application in several thermal engineering fields, including chemical processing, oil and gas industries, and waste heat recovery applications is notable for HTHE. Moreover, in the cooling application in power generation and geothermal usage [49], its necessity is increasing day by day. Although there are excellent opportunities for better heat transfer with this kind of heat exchanger, they are constrained by increased pressure drop. Therefore, the overall evaluation of thermal performance is crucial for achieving the intended practical use.

In this study, the designs have been proposed by keeping some parameters constant for proper analysis. These design constraints for all configurations are the pitch distance (P), the helix diameter (d_h) and the length of the pipe (L). Furthermore, it is crucial to note that the hydraulic diameter (D_H) is maintained at the same value for all geometries. Due to the impracticality of simultaneously restricting all geometric parameters, certain parameters are set to be free. Therefore, the length of the helix (L_1) and the number of turns are varying parameters to maintain the constraint parameters at the same values. Hence, altering the parameters should result in discernible variations in thermal performance and friction loss. Three unique designs are proposed in terms of variation in helix structure. Design-1 is a traditional helix-type heat exchanger. This design's helix diameter has been selected to be the average of the inner and outer helix diameters of the other designs (Design-2 and Design-3). The turn numbers and helix length are significantly more than the other two fundamental designs. Therefore, the length of the helix is 0.865 m and it has 17 twists. Considering Design-2, the concept of turning path is inspired by an existing work [20]. On a flat surface, two coils with differing diameters that are placed one inside the other are joined. These coils are vertically connected by curved pipes. The length of the helix is 0.45 m and it completes 9 turns. Design-3 consists of a body formed by two interconnected helices with two varying inner and outer helix diameters, which is the same as the value of Design-1. Table 1 provides comprehensive information on dimensions.

2.2. Considered cases

With the aforementioned fundamental designs, the effect of different inlet profiles has been combined to assess the overall thermo-fluid characteristics. These proposed inlet shapes are circular, square and oval, as depicted in Fig. 2 with exact dimensions. For each of the fundamental designs, there is a considered case with a proposed inlet shape. Therefore, a total of nine cases are tabulated in

Table 1
Dimension of all the cases.

Design 1		Design 2		Design 3	
Parameters	*Dimensions (m)*	*Parameters*	*Dimensions (m)*	*Parameters*	*Dimensions (m)*
Length of helix, L_1	0.865	Length of helix, L_1	0.4	Length of helix, L_1	0.3
Diameter of helix, d_h	0.13	Diameter of helix (inner & outer), (d_i & d_o)	0.170 & 0.10	Diameter of helix (inner & outer), (d_i & d_o)	0.170 & 0.10
Pitch value, P	0.05	Pitch value, P	0.05	Pitch value, P	0.05
Length of pipe, L	7.44	Length of pipe, L	7.44	Length of pipe, L	7.44
Turn number	17	Turn number (inner & outer)	9 & 9	Turn number (inner & outer)	6 & 13

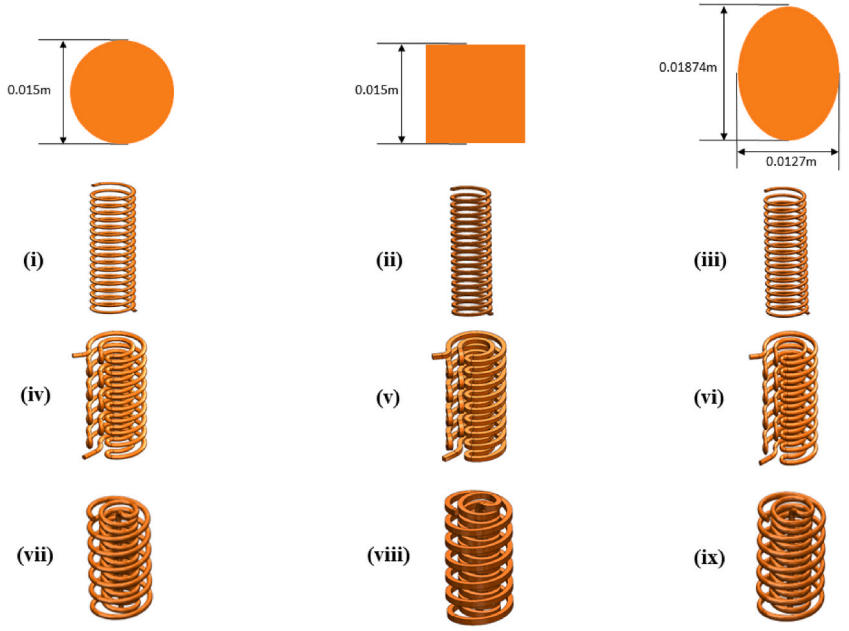

Fig. 2. Dimensions of the circular, square and oval cross-sectional profiles of the geometries with (i) Case 1, (ii) Case 2, (iii) Case 3, (iv) Case 4, (v) Case 5, (vi) Case 6, (vii) Case 7, (viii) Case 8 and (ix) Case 9.

Table 2
Number of cases and profiles.

Case No.	Fundamental Design	Type of Inlet Shape
01	Design 1	Circular
02	Design 1	Square
03	Design 1	Oval
04	Design 2	Circular
05	Design 2	Square
06	Design 2	Oval
07	Design 3	Circular
08	Design 3	Square
09	Design 3	Oval

Table 2. As the hydraulic diameter is the same for all the cases, the cross-section area varies. This hydraulic diameter is 0.015 m.

3. Mathematical formulations

3.1. Governing equations

The numerical study was carried out using Ansys Fluent. The Reynolds Averaged Navier-Stokes (RANS) model is used for evaluating the flow domain. This subsection provides an extensive synopsis of the basic concepts and mathematical expressions that apply to all conditions. The following expressions represent the fundamental governing equations [4].

- Continuity equation:

$$\frac{\partial(\rho u_i)}{\partial x_i} = 0 \tag{1}$$

- Momentum equation:

$$\frac{\partial(\rho u_i)}{\partial t} + \frac{\partial(\rho u_i u_j)}{\partial x_j} = \frac{\partial \rho}{\partial x_i} + \frac{\partial}{\partial x_j}\left(\mu \frac{\partial(u_i)}{\partial x_j} . \rho \overline{u_i' u_j'}\right) \tag{2}$$

- Energy equation:

$$\frac{\partial}{\partial x_i}(\rho T)+\frac{\partial}{\partial x_i}(\rho u_i T)=\frac{\partial}{\partial x_i}\left(\frac{\gamma}{C_p}.\frac{\partial T}{\partial x_i}\right) \tag{3}$$

In the equations above, the fluid's density in (kg m^{-3}), is indicated by the ρ symbol, and the fluid's specific heat per Kelvin ($Jkg^{-1}K^{-1}$) is shown by C_p. The x-direction velocities expressed in m/s are denoted by the symbol u_i. Finally, T is the fluid's temperature, expressed in K.

Using the k-ε model, the flow turbulence has been captured. This framework has been modified for looping streams as well as horizontal shear layer modelling. It is frequently used in streams with free shear layers that have a smaller pressure gradient. The following representation is presented as the k-ε model [4,50]:

Turbulence *k-ε* equation sets are as follows:

$$\frac{\partial}{\partial t}(\rho k)+\frac{\partial}{\partial x_i}(\rho k u_i)=\frac{\partial}{\partial x_j}\left[\left(\mu+\frac{\mu_t}{\sigma_k}\right)\frac{\partial k}{\partial x_j}\right]+G_k+G_b-\rho\varepsilon-Y_M-S_k \tag{4}$$

And,

$$\frac{\partial}{\partial t}(\rho \varepsilon)+\frac{\partial}{\partial x_i}(\rho \varepsilon u_i)=\frac{\partial}{\partial x_j}\left[\left(\mu+\frac{\mu_t}{\sigma_\varepsilon}\right)\frac{\partial \varepsilon}{\partial x_j}\right]+C_{1\varepsilon}\frac{\varepsilon}{K}(G_k+C_{-\varepsilon}G_b)-C_{2\varepsilon}\rho\frac{\varepsilon^2}{k}+S_\varepsilon \tag{5}$$

In these two equations, the component of velocity is denoted *by* u_i, the rate of deformation is denoted by E_{ij}, and eddy viscosity is denoted by μ_t. Y_M reflects the impact of varying dilatation in compressible turbulence on the total dissipation rate. S_k and $S_\mathcal{E}$ are denoted as user-defined source terms.

3.2. Mathematical equations

A three-dimensional steady-state flow computational technique is adopted in this investigation. Water is used as the main fluid for the performance testing. As the Reynolds number has a considerable effect on the control of the fluid's flow condition, it is chosen within a wide functional range of 5000–25000 for this study. The flow regime within helical tubes is turbulent, which, in conjunction with the tubes' helical shape, induces a continuous swirling motion as the fluid traverses the tube. This swirling effect enhances the mixing and heat transfer characteristics of the flow. It is necessary to evaluate multiple factors to determine how effective the newly presented geometries are. The factors encompass features related to thermal properties, hydraulic properties, and entropy formation. The formula to evaluate the Nusselt number (*Nu*), is presented below, which is the dimensionless quantity employed to characterize the features of heat transport [27]:

$$Nu=\frac{hD_h}{k} \tag{6}$$

In this equation, the surface heat transfer coefficient (W/m^2 K) is denoted by h, the thermal conductivity (W/m-K) using k and the hydraulic diameter (m) is denoted by D_h.

Heat transfer coefficient (h) is computed from Ref. [4]:

$$h=\frac{q_{wall}}{LMTD} \tag{7}$$

Where wall heat flux (W/m^2) is denoted by q_{wall}. The Log Mean Temperature Difference (LMTD) approach is used in the present investigation to determine the wall heat flow quality because it maintains even surface temperature instances. The equation for LMTD is as follows [4]:

$$LMTD=\frac{\Delta T_1-\Delta T_2}{\ln\left(\frac{\Delta T_1}{\Delta T_2}\right)} \tag{8}$$

In this case, the temperature difference that exists between the wall's mean temperature and the location of the entrance is indicated by ΔT_1, and the difference in temperature between the outermost layer of the wall and the outflow is indicated by ΔT_2. To calculate the heat exchanger's (HX) friction factor (f), the pressure drop is first calculated and then used in the following expression [3]:

$$f=\frac{2D_h\Delta p}{L\rho V^2} \tag{9}$$

To perform a study on entropy generation, the rate of generated entropy per unit of volume is integrated over the full volume (V) to find the total rate of the generation of entropy. Thus, the expression for the entropy generation is [13]:

$$S_g = \int_V s_g dV \tag{10}$$

3.3. Ternary hybrid nanofluid properties

The usage of nanofluids in different engineering applications is increasing with time. Introducing the nanoparticle into the base fluid greatly enhances its heat conduction capacity. However, this can lead to increased viscosity, hindering the motion of the fluid. Therefore, to solve this concern, the concentration of the used nanoparticles needs to be adjusted depending on the engineering application. Due to upgraded thermal properties, ternary hybrid nanofluids are becoming more and more relevant in various studies. A prior study [51] recommends its use for applications in applied thermal engineering. This nanofluid composition requires mixing three different nanoparticles into the main fluid wherein the nanoparticles are uniformly distributed due to their minuscule dimensions. It is very important to mention that, regarding the novelty of this research, no studies have been conducted on the utilization of ternary hybrid nanofluid (THNF) in helical-type heat exchangers. Due to the increased secondary flow, the helical heat exchanger experiences higher heat transmission. Therefore, incorporating THNF can improve the system's overall output. In this work, THNF is considered to exist as a homogeneous single phase. The single-phase model for nanofluids in helical tube heat exchangers simplifies simulations, requiring less computational power and providing stable numerical solutions. However, it may not accurately capture micro-level interactions, relies on potentially invalid assumptions, and is unsuitable for detailed analyses where particle-fluid interactions are critical [52,53]. Moreover, the nanoparticles are evenly distributed in the base fluid with no sedimentation, to attain uniform properties and consistent behaviour of the nanofluid.

At 303K, the nanofluids' thermophysical characteristics have been established. A total of six distinct THNFs are chosen for the comprehensive comparison analysis, with a volume proportion of 0.03 %. Three metal oxides (Al_2O_3, CaO, and ZnO) are considered to be nanoparticles because of their promising thermophysical properties and high degree of stability in the base fluid. Moreover, the study incorporates graphene and carbon nanotube (CNT) owing to their elevated thermal conductivity characteristics and high stability in high-temperature conditions. However, these nanoparticles are known for their higher viscosity which causes additional pressure loss. Moreover, potential fouling is a great concern while using these nanoparticles. These nanoparticles have been used in the existing literature works [41–44]. The thermophysical properties of the nanofluids have been determined under steady-state conditions and at a temperature of 303K. No thermal radiation and magnetic effect is taken into account. The list of THNFs for this study is given in Table 3.

For a ternary hybrid nanofluid, the equation to determine density and specific heat is derived using the mixing model [54]. These equations for the ternary hybrid nanofluid are provided below:

$$\rho_{hnf} = \rho_{np1}\phi_{np1} + \rho_{np2}\phi_{np2} + \rho_{np3}\phi_{np3} + \left(1 - \phi_{np1} - \phi_{np2} - \phi_{np3}\right)\rho_{BF} \tag{11}$$

$$\left(\rho_{hnf}C_p\right)_{hnf} = \rho_{np1}C_{p_{np1}}\phi_{np1} + \rho_{np2}C_{p_{np2}}\phi_{np2} + \rho_{np3}C_{p_{np3}}\phi_{np3} + \left(1 - \phi_{np1} - \phi_{np2} - \phi_{np3}\right) \times \left(\rho_{BF}C_{p_{BF}}\right) \tag{12}$$

The shape of nanoparticles, in addition to the volume fraction, significantly influences the evaluation of thermos-physical properties in hybrid nanofluids [55,56]. Based on the shape factors of the nanoparticles, thermal conductivity and viscosity are mostly determined in the existing literature. The shapes under consideration are spherical, cylindrical, and platelet, as indicated in Table 4 in relation to the nanoparticles. The formula for determining a ternary hybrid nanofluid's effective thermal conductivity is given below [42]:

$$\frac{K_{hnf}}{K_{BF}} = \frac{k_{np1} + (n-1)k_{BF} + (n-1)\phi\left(k_{np1} - k_{BF}\right)}{k_{np1} + (n-1)k_{BF} - \left(k_{np1} - k_{BF}\right)} \tag{13}$$

Here, when a nanofluid is made up of cylindrical, platelet, and spherical type nanoparticles, its thermal conductivity can be written as [42]:

$$\frac{K_{nf_1}}{K_{bf}} = \frac{k_{np1} + 2k_{BF} + 2\phi\left(k_{np1} - k_{BF}\right)}{k_{np1} + 2k_{BF} - \left(k_{np1} - k_{BF}\right)} \text{ (Spherical shape, nanoparticle 1)} \tag{14}$$

Table 3
Ternary hybrid nanofluid (THNF) details [43,44].

Nanofluid Name	Nanofluid Composition
THNF 1	Al_2O_3+CaO + ZnO
THNF 2	Al_2O_3+CaO + Graphene
THNF 3	Al_2O_3+CaO + CNT
THNF 4	Al_2O_3+ZnO + CNT
THNF 5	Al_2O_3+ZnO + Graphene
THNF 6	Al_2O_3+CNT + Graphene

Table 4
Nanoparticle and water thermophysical properties [43,44].

Material	(Kg/m^3)	(J/kg-K)	(W/m-K)	(Kg/m-s)	Morphology
Al_2O_3	3970	765	40	–	Spherical
ZnO	5600	495.2	1.3	–	Cylindrical
CaO	3320	783	2.25	–	Cylindrical
Graphene	2200	790	5000	–	Platelet
CNT	2100	410	3007.4	–	Cylindrical
Water	995.18	4070.2	0.619	0.000777	–

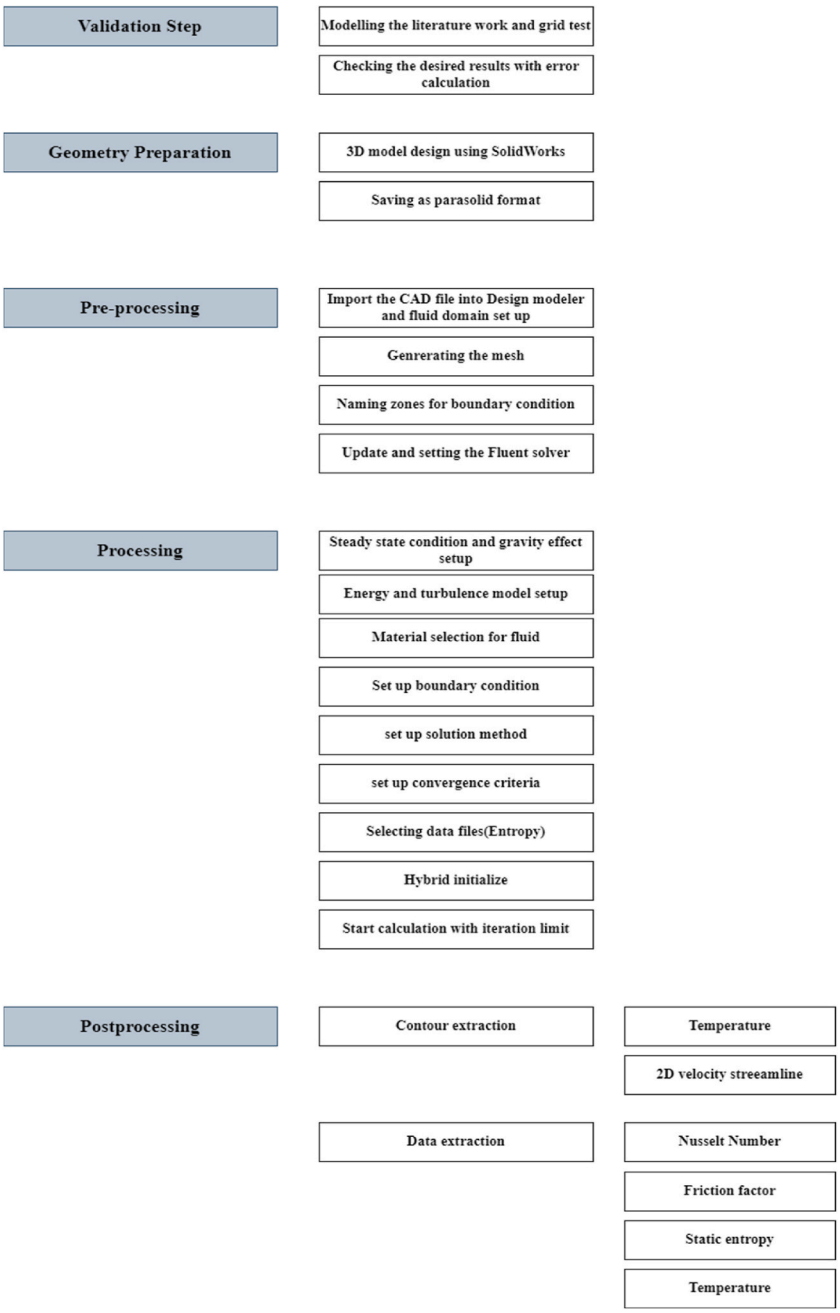

Fig. 3. The overall numerical methodology of the current study.

$$\frac{K_{nf_2}}{K_{BF}} = \frac{k_{np2} + 3.9k_{BF} + 3.9\phi\left(k_{np2} - k_{BF}\right)}{2k_{np1} + 3.9k_{BF} - \left(k_{np2} - k_{BF}\right)} \text{ (Cylindrical shape, nanoparticle 2)} \tag{15}$$

$$\frac{K_{nf_3}}{K_{BF}} = \frac{k_{np3} + 4.7k_{BF} + 4.7\phi\left(k_{np3} - k_{BF}\right)}{2k_{np1} + 4.7k_{BF} - \left(k_{np3} - k_{BF}\right)} \text{ (Platelet shape, nanoparticle 3)} \tag{16}$$

Similarly, the determination of viscosity for nanoparticles with different forms is designated as [42],

$$\mu_{nf_1} = \mu_{BF}\left(\phi^2 + 2.5\phi + 1\right) \text{ (Spherical shape, nanoparticle 1)} \tag{17}$$

$$\mu_{nf_2} = \mu_{BF}\left(904.4\phi^2 + 13.5\phi + 1\right) \text{ (Cylindrical shape, nanoparticle 2)} \tag{18}$$

$$\mu_{nf_3} = \mu_{BF}\left(612.6\phi^2 + 37.1\phi + 1\right) \text{ (Platelet shape, nanoparticle 3)} \tag{19}$$

The nanoparticles ZnO, CaO, and CNT are spherical in shape, whereas Al_2O_3 and Graphene have spherical and platelet shapes, respectively. The equation below incorporates all the values of the different nanofluids for the final calculation of the viscosity of the ternary hybrid nanofluid [42,43].

$$\mu_{hnf} = \frac{\left(\mu_{nf_1}\phi_{np1} + \mu_{nf_2}\phi_{np2} + \mu_{nf_3}\phi_{np3}\right)}{\phi} \tag{20}$$

The equation for calculating the thermal conductivity of the ternary hybrid nanofluid is provided below: [29,57];

$$k_{hnf} = \frac{\left(k_{nf_1}\phi_{np1} + k_{nf_2}\phi_{np2} + k_{nf_3}\phi_{np3}\right)}{\phi} \tag{21}$$

4. Numerical methodology

In this section, numerical methods are employed, boundary conditions are established, meshing criteria, including grid selection, are determined, and validation is carried out.

4.1. Method

With the use of Ansys Fluent, the computational model was solved via the finite volume method. One of the requirements for the solution was to use a coupled solver that operated under pressure. Because the SIMPLE technique may be used to connect the momentum and continuity equations, it is being chosen to handle heat and fluid transfer issues. For spatial discretization, the second-order upwind technique was selected to increase the precision of the results. The least squares cell-based method was the gradient choice selected as the most suitable technique for addressing the computational model. The equation for energy was set with a limit of 10^{-6} concerning the convergence threshold when the other features were fixed at a constraint of 10^{-4}. A comprehensive synopsis of the numerical techniques is offered in Fig. 3 to aid in understanding.

4.2. Boundary conditions

The fluid's heating state was taken into consideration in this simulation problem. The flow of fluid is taken to be in a steady state condition for the CFD scenarios [58]. The boundary wall is assumed to be at a constant temperature of roughly 368K. The fluid flowing through the opening in the helical pipe has a temperature of roughly 298K. Zero-gauge pressure is used as the input for the outlet pressure. The Reynolds number has been changed from 5000 to 25000 in order to investigate the flow influence on heat transmission

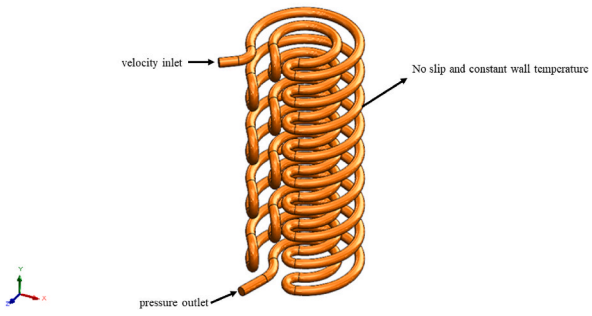

Fig. 4. Geometry with boundary conditions.

characteristics. Every scenario was simulated for five different velocities. The turbulence effect was represented by the k-ε model. The no-slip condition was taken into account at the wall side. The value of 9.8 ms^{-2} was obtained by applying the gravitational influence in the negative Y-axis orientation. Fig. 4 represents the boundary conditions with proper marking. Six ternary hybrid nanofluids (THNFs) have been selected for the simulations in the nanofluid flow study. 343K was chosen as the applied constant wall temperature. A starting temperature of 303K was taken into consideration. The Reynolds number range was established as fixed. The velocities were altered for the same Reynolds number as a result. For convenience, all the boundary conditions are tabulated in Table 5.

4.3. Multi-criteria decision-making (MCDM) approach

Multi-criteria decision-making (MCDM) refers to a statistical methodology used to determine the most important parameters by employing both qualitative and quantitative techniques. This strategy distinguishes between the beneficial and non-beneficial factors in order to facilitate the criteria for decision-making. The study utilized MCDM to ascertain the optimal performance among various helical heat exchanger designs. Due to the distinct design configurations and varying inlet profile shapes of the proposed helical tubes in this study, there is no typical smooth or standard helical tube case to be evaluated to determine the thermal performance factor. Therefore, to address the issue, the MCDM model has been chosen to evaluate the overall performance of the proposed cases. Initially, a matrix is constructed using the result parameters of the proposed designs. This matrix is named a decision matrix. All the values in this matrix can be categorized into two sections, beneficial and non-beneficial. The parameters which are considered to be good for the system are in the category of beneficial values and which are considered to be bad are designated as non-beneficial values. For example, the Nusselt number and the outlet temperature of the fluid in HTHE are beneficial to heat transfer enhancement whereas friction factor and entropy generation are non-beneficial to the system. Beneficial values are anticipated to be higher and non-beneficial values are to be lower. Therefore, each value of this matrix is called a performance value. After the decision matrix is formed, it needs to be transformed into a normalized decision matrix. Therefore, all the specific beneficial criteria need to be divided by their maximum values and all the specific non-beneficial criteria need to be divided by their minimum values. This process converts the beneficial and non-beneficial criteria to normalized beneficial and non-beneficial criteria. After this, weighting values are assigned to the normalized beneficial and non-beneficial criteria to form a weighted normalized matrix. The total of the assigned weighting values must be equal to 100. At last, all the criteria having the weighted normalized performance values are summed up for each design case to determine the performance score. The performance score is the main representation of the thermal performance factor of each design. In Fig. 5, the consequent steps of the MCDM procedure are depicted with a flow chart.

4.4. Mesh selection and Grid Independence Test

In the present study, Ansys Mechanical was employed to build mesh elements for each configuration due to the ability to be precise, and flexible and enhance user interface and engagement with the device. The fluid domain was covered by a tetrahedral mesh with 0.003 mm element size, which was effective in capturing both the flow structure and the thermal characteristics. Using tetrahedral meshing, the element numbers utilized in the present study is 166665 elements (Fig. 6).

Table 6 demonstrates the use of a Grid Independence Test (GIT) to determine the optimal number of mesh elements needed to represent flow dynamics effectively while keeping processing costs reasonable. The computed deviation in outlet temperature for 166,665 elements is 0.26 %, suggesting a highly reliable performance. Compared to the other designs, this specific mesh size demonstrates notable convergence in the outlet temperature. Therefore, a total of 166665 pieces that required a relatively low amount of computational work were selected for execution.

4.5. Model validation

In order to determine the reliability of the numerical model, the Nusselt number and friction factor for different velocities across a helical heat exchanger have been compared to the computational results of Zhang et al. [26] in Fig. 7(a and b). For the Nusselt number, 7.2 % is the most deviation value from the literature. In terms of friction factor, the maximum deviation value is 5.66 %. Therefore, it

Table 5
Boundary conditions for the computational domain.

Name	Conditions for Simulations	
Inlet	***Momentum*** v = inlet velocity with respect to Re = 5000–25000, according to the channel's hydraulic diameter, $D_h = 0.015m$	***Energy*** Inlet temperature for water, $T_{in1} = 298\ K$ Inlet temperature for nanofluid, $T_{in2} = 303\ K$
Helical Tube Heat Exchanger	No slip condition	***Boundary Condition*** Constant temperature at pipe wall for water, $T_{wall1} = 368$ K Constant temperature at pipe wall for nanofluid, $T_{wall2} = 343$ K
Outlet	$P_{out} = 0$, pressure outlet	
Gravity	g = 9.8 ms^{-2}	
Turbulence Model	k-ε realizable model	

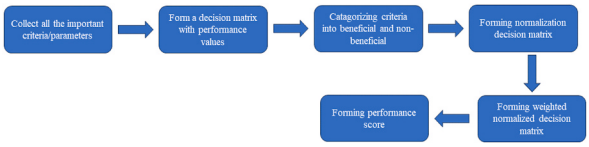

Fig. 5. Multi-criteria decision making (MCDM) procedure Flowchart.

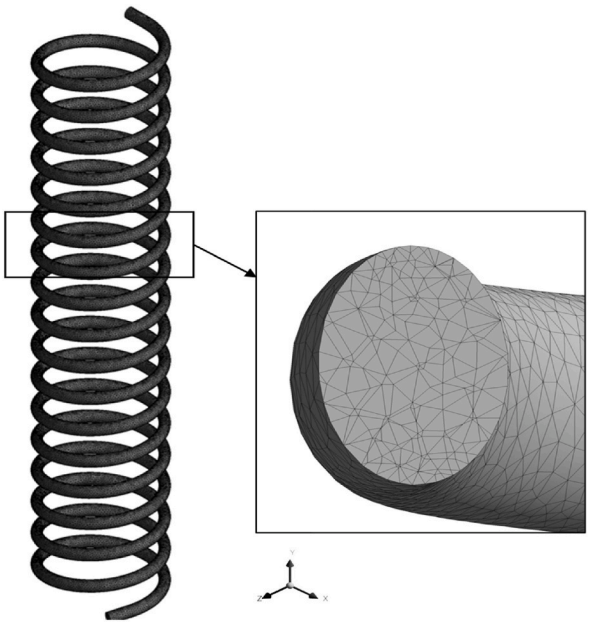

Fig. 6. Detailed view of the generated mesh.

Table 6
Grid Independence test.

Elements Number	Outlet Temperature (T_o)	$\frac{T_{o(i+1)} - T_{o(i)}}{T_{o(i+1)}}$
129,928	360.8533	–
587,995	362.5709	0.004737
792,444	365.1798	0.007144
166,665	**366.1219**	**0.002573**
2,445,923	366.2894	0.00046

can be stated that the validation is in an acceptable range. Another validation is conducted with the experimental correlation of Manlapaz and Churchill [59] for a smooth helical tube, given in Fig. 7(c). The validation model is satisfied with a maximum error of 4.3 %.

5. Results and discussions

The following section discusses the heat transfer and hydraulic performance of the considered nine helical heat exchanger cases. The velocity streamline, temperature profile, 3D streamline, the Nusselt number, friction factor and entropy generation plot varying the Reynolds number have been illustrated. The MCDM was also applied in order to decide the best-performed heat transfer configurations.

5.1. Effect on streamlines

Fig. 8 depicts the velocity streamline profiles at the outflow section for each of the nine configurations. Two vortices have been seen in the Design 1 helical heat exchanger cases. These two vortices provide enhanced fluid flow mixing. Helical heat exchangers surpass other types of heat exchangers, such as straight pipes, due to their greater performance. The level of mixing in straight pipes is less

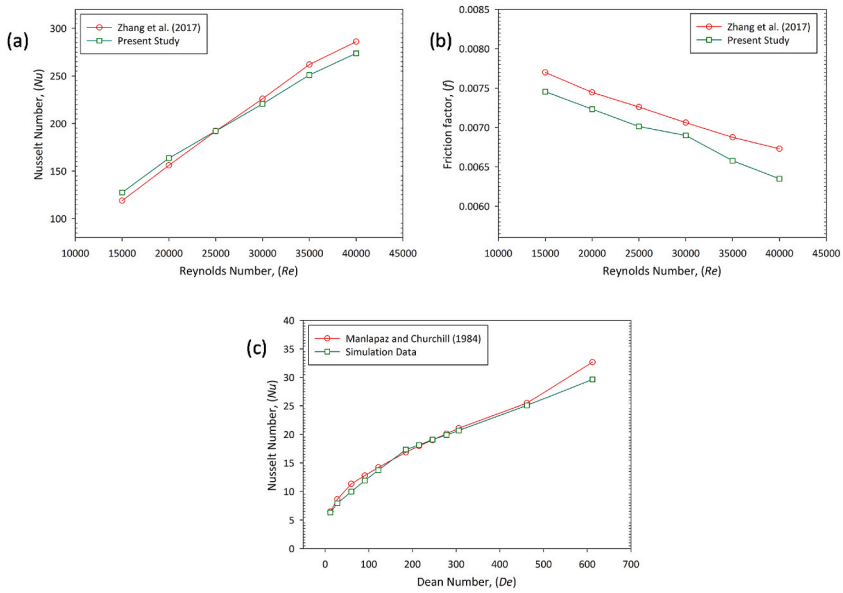

Fig. 7. Validation of the current model with (a, b) existing numerical literature of Zhang et al. [21] and (c) Experimental correlation of Manpalaz and Churchill [59].

significant compared to helical heat exchangers. The presence of vorticities also contributes to enhanced heat dissipation, a topic that will be further explored in subsequent sections. In Design 2 configurations, three distinct profiles exhibit two velocities at the cross-sectional plane. The fluid velocity is greater in the areas near to the vortex core. However, the velocity is lower in the wall area of the heat exchangers. In the Design-3 design, the velocity streamlines vary from the other two configurations. The presence of single vorticities in the cross-sectional plane is seen for all three profiles under consideration. However, the magnitude of velocity is identical to the preceding two configurations. The reduced velocity is also seen in the vicinity of the walls. The 3D streamlines for the whole fluid domain for all nine configurations have been illustrated in Fig. 9.

5.2. *Effect on temperature distributions*

The temperature distributions throughout the cross-sectional profile for the nine considered helical geometries have been presented in Fig. 10. A Reynolds number (Re) of 25000 has been selected for this analysis. The temperature at the exterior wall zone is higher than the temperature in the center section, which is noticeably lower. Comparing the temperature distributions for different shapes of the profile, it is found that the temperature is lower for the square-shaped geometry compared to oval and circular shapes. Because the square shape possesses a greater ratio of surface area to volume, resulting in improved convective heat transfer and decreased temperature. Design 2 provides a higher temperature distribution than Design 1. This is because Design 2 has two coils with differing diameters placed one inside the other and joined by curved pipes. This design variation enhances fluid mixing and promotes uniformity of the temperature distribution in the radial direction, resulting in a higher temperature distribution compared to Design 1. The temperature distribution is almost identical for both circular and oval-shaped cross-sections. The precise magnitude of the outlet temperature is depicted in the later section.

5.3. *Effect on Nusselt number*

The heat transfer performance has been assessed for all these nine heat exchangers. The Nusselt number for the considered cases has been calculated, varying the Reynolds number (From Re = 5000 to Re = 25000), which is illustrated in Fig. 11. It has been found that the heat transfer rate increases as the fluid velocity inside the heat exchanger increases. This type of occurrence can be observed for all the shapes and configurations. This phenomenon occurs as a result of heightened turbulence and agitation, which leads to improved mixing and thermal transfer. In the Re = 25000 scenario, the Nusselt number rises by 3.23 times relative to the lower Reynolds number, Re = 5000. Therefore, to get a higher rate of heat transfer, the velocity plays a crucial role. Additionally, there is a discrepancy in the thermal performance of the different heat exchangers. Design 1 with an oval shape demonstrates the highest heat transmission rate compared to the other cases. The oval shape improves the convection of heat and minimizes the generation of entropy. An almost similar result was obtained from Design 2, which is oval cross-section geometry. For the lower Reynolds number, Design 3 with an oval cross-section provides the third-highest heat transfer performance. When compared to circular and square-shaped geometries, it is found that oval-shaped geometries function better. The lower thermal performance is visible for square-shaped geometries. The graphs indicate that Design 3 with a square cross-section configuration, has the lowest heat transmission.

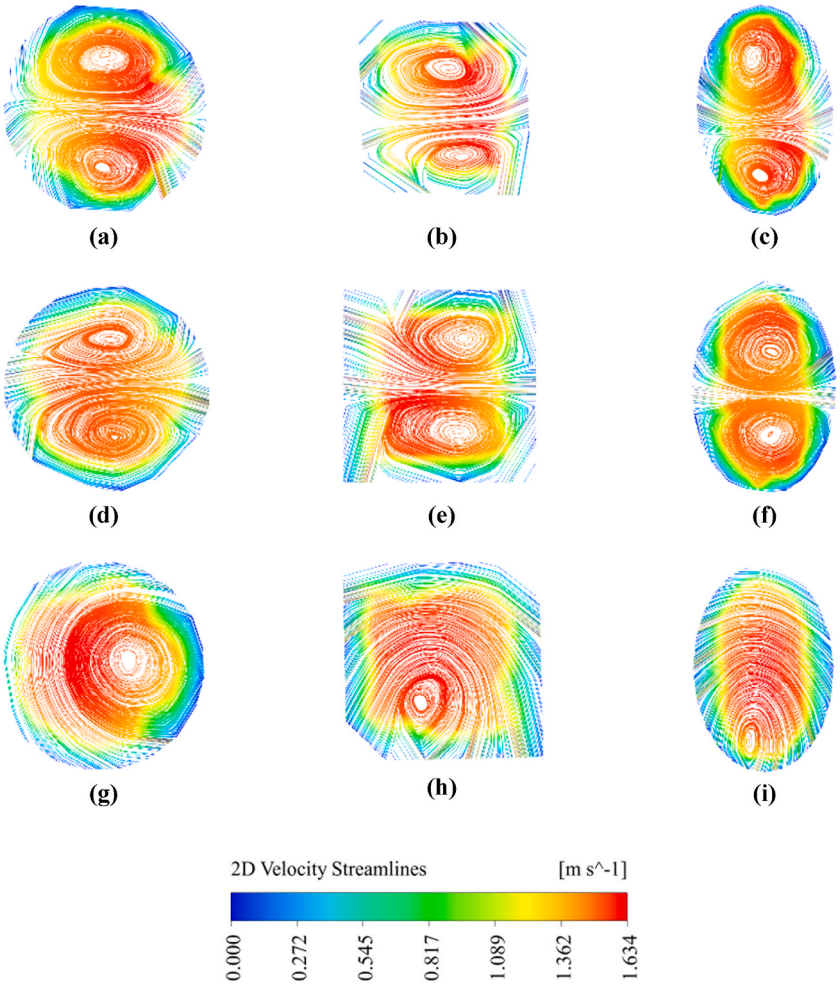

Fig. 8. 2D Streamline contour of the outlet plane for (a) Design-1 Circular, (b) Design-1 Square, (c) Design-1 Oval, (a) Design-2 Circular, (b) Design-2 Square, (c) Design-2 Oval, (a) Design-3 Circular, (b) Design-3 Square, (c) Design-3 Oval at Re 25000.

5.4. Effect on outlet temperature

The thermal and hydraulic efficiency of the chosen heat exchangers has been assessed and compared in this investigation using heating settings. Consequently, thermal energy is transmitted to the fluid, causing a rise in its temperature. Due to variations in the geometrical arrangement, the exit temperature of the fluid differs across all scenarios. The correlation between the Reynolds number and the output temperature for various heat exchangers is shown in Fig. 12. It has been noted that when the fluid velocity increases, the output temperature decreases. Additionally, variations in outlet temperature may be seen for various cross-sectional profiles. The graphical representation indicates that oval-shaped heat exchangers often exhibit greater output temperatures, whereas those with square-shaped cross sections have the lowest temperatures. The reason is the oval shape elevates the convection of heat and minimizes the generation of entropy. It has been shown that for cross sections with comparable shapes, such as oval, Design 3 yields a greater fluid temperature at the outlet. Design 1 has a somewhat lower output temperature. Upon comparing all nine examples, it is seen that Design 2, with an oval profile, yields the greatest outlet temperature, while the cases of Design 1, having a square profile, result in the lowest outlet temperature.

5.5. Effect on friction factor

The friction factor is a critical characteristic that influences the overall performance of the heat exchanger system. Fig. 13 illustrates how the friction factor changes with the Reynolds number across all nine cases. The objective is to test the hydraulic performance considering the pressure drop. Observations have shown that the friction factor reduces in proportion to the increase in the Reynolds number. These tendencies are observable across all scenarios. In comparison to Designs 1 and 3, it is clear that Design 2 has the highest friction factor. This is the conclusion that can be drawn from the visualization of the plot. This is due to its distinctive shape including

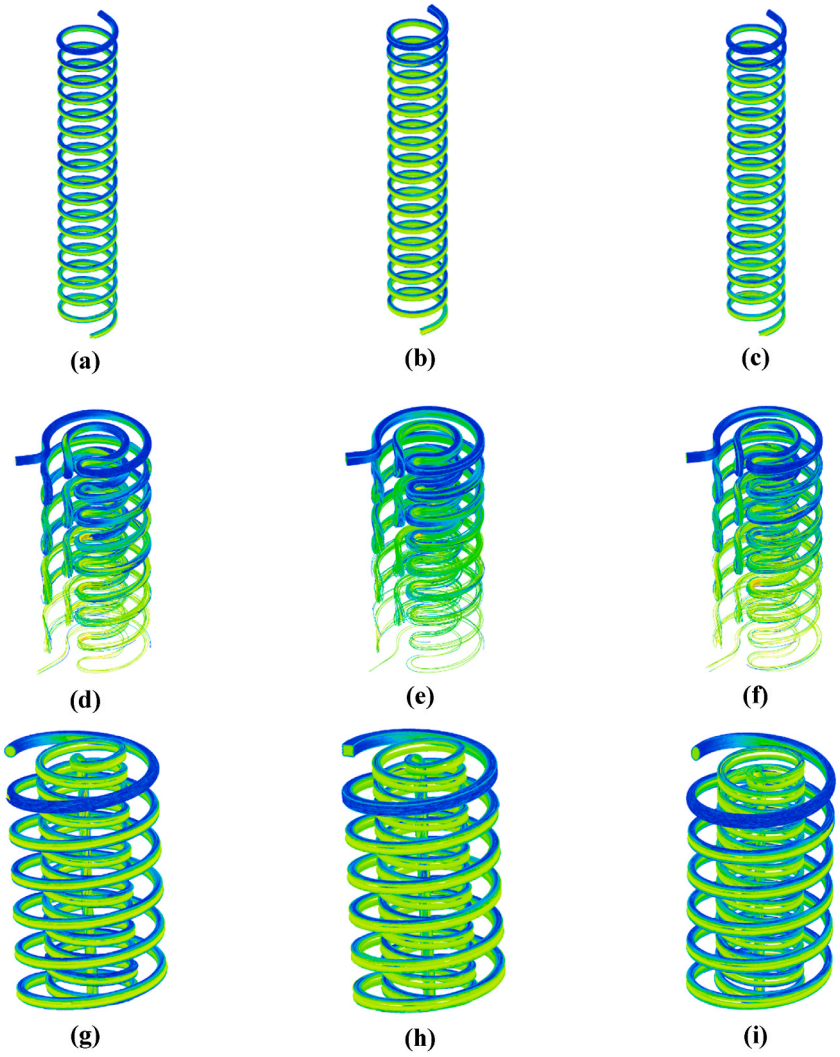

Fig. 9. 3D Streamline contour of the outlet plane for (a) Design-1 Circular, (b) Design-1 Square, (c) Design-1 Oval, (a) Design-2 Circular, (b) Design-2 Square, (c) Design-2 Oval, (a) Design-3 Circular, (b) Design-3 Square, (c) Design-3 Oval at Re 25000.

two coils with varying diameters. This design modification improves the blending of fluids and ensures that the temperature is evenly distributed in all directions, leading to an increased friction factor. Design 1 configurations exhibit the least amount of friction. Upon comparing the cross-sectional profiles, it is evident that the square-shaped profile yields a lower friction factor. Conversely, a circular shape profile yields a greater friction factor. These statements hold true for all three design variants. Among all the situations, Design 2, with a circular cross-section, has the greatest friction factor. However, the design with a square cross-section shape, known as Design 1, exhibits the lowest friction factor. The friction factor for Design 2 with a circular cross-section is 48 % more than the friction factor for Design 1 with a square cross-section profile.

5.6. Effect on entropy

The static entropy for the nine geometrical heat exchanger scenarios is shown in Fig. 14 for different Reynolds values. It is observed that with the increase in Reynolds number, the static entropy decreases. This is due to is due to increased turbulence, reduced viscous dissipation, and decreased entropy generation. Therefore, lower entropy generation is found for a high Reynolds number, specifically for this analysis with Re = 25000. Entropy generation varies with geometrical configurations, and it is found that entropy generation is greater for Design 2 cases. However, lower entropy is found for the Design 1 configuration. With the variation in the cross-sectional profile, entropy generation changes. It is observed that higher entropy generation is found for an oval-shaped heat exchanger, while the lower entropy value is found for a square-shaped cross-sectional profile. The higher entropy generation is a consequence of the oval shape's smaller surface area-to-volume ratio, which causes less uniform fluid flow and mixing. The square-shaped profile's greater ratio of surface area to volume, more consistent fluid flow, and reduced pressure drops all contribute to its decreased creation of

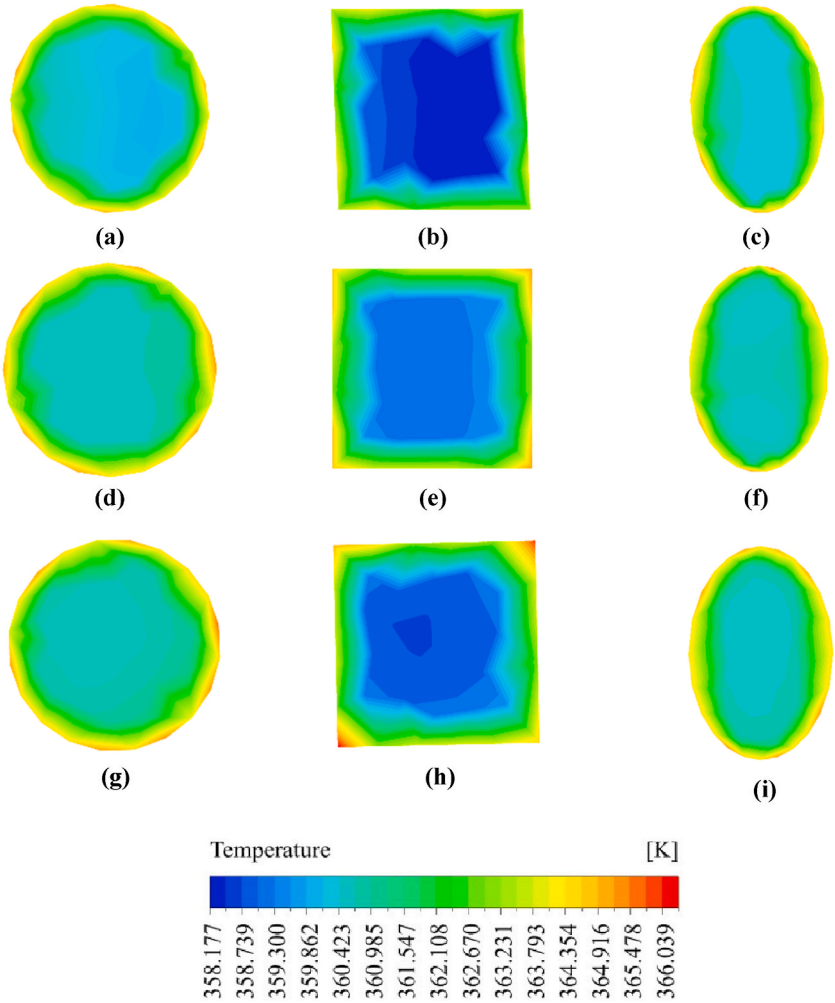

Fig. 10. Temperature contour of the outlet plane for (a) Design-1 Circular, (b) Design-1 Square, (c) Design-1 Oval, (a) Design-2 Circular, (b) Design-2 Square, (c) Design-2 Oval, (a) Design-3 Circular, (b) Design-3 Square, (c) Design-3 Oval at Re 25000.

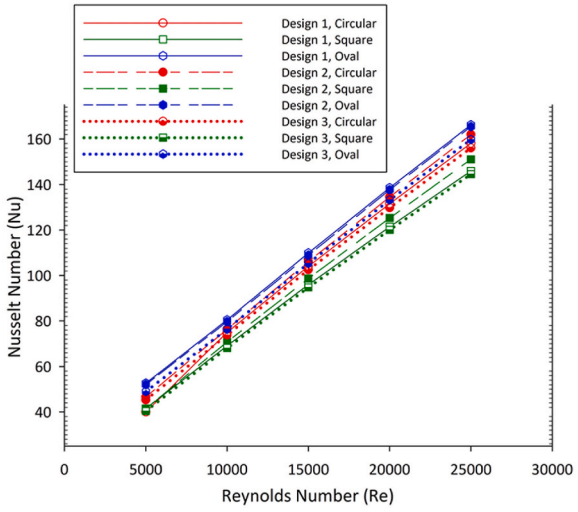

Fig. 11. Nusselt number comparison of the nine cases across Re 5000-25000.

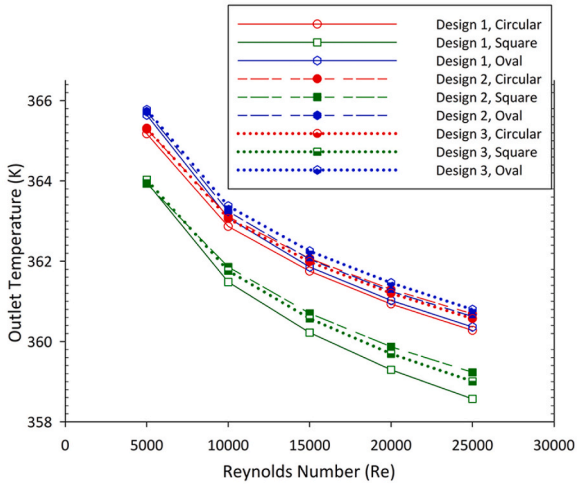

Fig. 12. Outlet temperature comparison of the nine cases across Re 5000-25000.

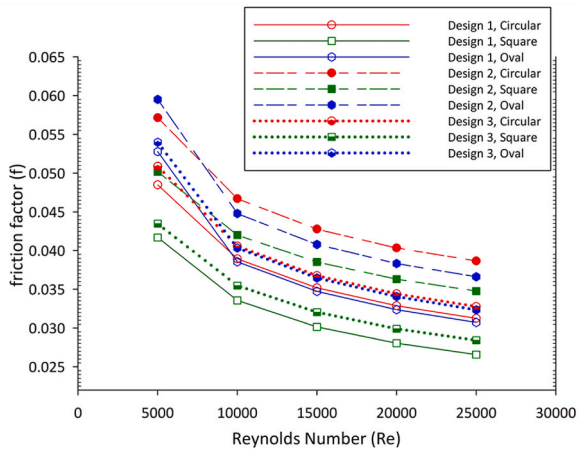

Fig. 13. Friction factor comparison of the nine cases across Re 5000-25000.

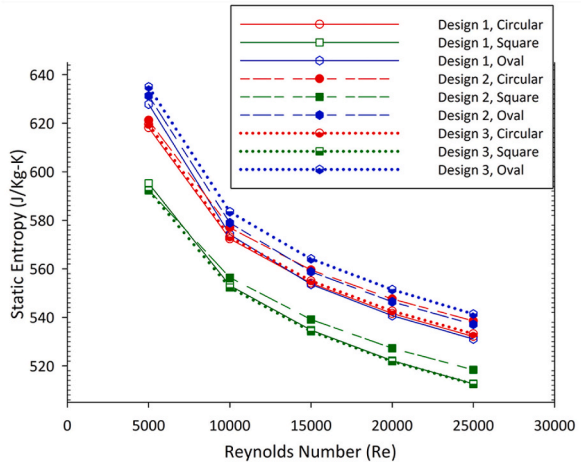

Fig. 14. Static entropy comparison of the nine cases across Re 5000-25000.

entropy. Considering all cases, the highest entropy value is found for Design 3 with oval shape geometry at Re = 5000. Conversely, Design 3 with a square-shaped configuration yields the lowest entropy value at Re = 25000. The entropy generation is 5 % lower for Design 3 with a square shape configuration at Re = 25000 compared to the case of Design 3 with oval shape geometry at Re = 5000.

5.7. Multi-Criteria Decision Making (MCDM) analysis for evaluating performance of HHX

This section introduces the incorporation of Multi-Criteria Decision Making (MCDM) to determine the overall performance of proposed HHX cases. Sample calculation tables are provided, taking into account a Reynolds number of 5000. The parameters in the table are categorized based on their impact on the heat transfer rate, distinguishing between beneficial and non-beneficial parameters. The Nusselt number (*Nu*), friction factor (*f*), outlet temperature (T_{out}), and entropy (S_g) have been included in the analysis. Since the increment of *Nu* and T_{out} is beneficial to raise the heat transmission rate and lower f and S_g is desired to increase the thermal performance, the beneficial and non-beneficial criteria have been set accordingly. Hence, in Table 7, the beneficial and non-beneficial parameters formed a decision matrix. From this decision matrix, the highest beneficial performance values in terms of *Nu* and T_{out} are 52.650 and 365. 773. In addition to that, the lowest values in the category of non-beneficial criteria are identified to be 0.0417 and 592.2845 for friction factor and entropy generation, respectively. Consequently, the normalized decision matrix, given in Table 8, is formed by dividing all the beneficial performance values with the highest value of the *Nu* and T_{out} criteria, accordingly and the lowest value for the *f* and S_g is divided by the performance values of both non-beneficial criteria. In the next step, a weightage value was multiplied by the normalized beneficial and non-beneficial values to construct a weighted normalized decision matrix (Table 9). The weightage value has been selected as 0.25 for all the considered criteria. At last, all the weighted normalized criteria (beneficial and non-beneficial) for a particular case have been added, resulting in a performance score. This performance score refers to the simultaneous effect of heat transfer increment, pressure drop and entropy generation for each case when the Reynolds number is 5000. Additionally, Fig. 15 illustrates the performance score of the considered cases for illustrates the performance score of the considered cases for various Reynolds number (Re=5000-25000).

5.8. Hydrothermal performance using ternary hybrid nanofluids

Design 1 with a square cross-sectional profile is identified as the most efficient heat exchanger by the MCDM. As a result, various nanofluids have been utilized to improve thermal performance, as indicated in Table 3. Each nanofluid is composed of a combination of three distinct nanoparticles, with water serving as the foundation fluid. The thermal performances of these Ternary hybrid nanofluids exhibit variations. Fig. 16(a) illustrates the alteration of the Nusselt number for six different nanofluids as the Reynolds number changes (Re = 5000 to 25000). The Nusselt number is shown to rise with an increase in the Reynolds number. The performance difference among the nanofluids is noticeable in situations with elevated Reynolds numbers. The THNF-6 (Al_2O_3+CNT+Graphene) has superior heat transfer capability compared to other nanofluids. Because the combination of these materials has ensured higher thermophysical properties such as thermal conductivity. Nevertheless, THNF-1 (Al_2O_3+CaO+ZnO) has the most minimal heat transfer rate. However, for situations with lower Reynolds numbers, the thermal performance is nearly identical. Fig. 16(b) depicts the comparison of friction factors. It is evident that THNF-5 (Al_2O_3+ZnO+Graphene) exhibits the highest friction factor value, while THNF-2 (Al_2O_3+CaO+Graphene) demonstrates the lowest. Fig. 16(c) illustrates the correlation between the output temperature and the Reynolds number regarding all six nanofluids. As the Reynolds number increased, the exit temperature decreased. It has been discovered that THNF-4 yields the highest temperature of the nanofluid at the outflow. Conversely, the THNF-2 (Al_2O_3+CaO+Graphene) provides the lowest value. The calculation of entropy generation is also performed for the aforementioned scenarios, and the results are shown in Fig. 16(d). As the Reynolds number grows, the static entropy generation reduces. The THNF-3 (Al_2O_3+CaO+CNT) exhibits the highest static entropy value, whereas the THNF-1 (Al_2O_3+CaO+ZnO) demonstrates the lowest.

6. Conclusions

The highlight of this study is the performance of comparative analysis on nine distinct helical tube heat exchangers with three inlet profiles, namely circular, square, and oval, and three different shapes of helix. After that, the obtained best case was further studied by

Table 7
Decision matrix table.

Re	Cases	*Nu*	f	T_{out}	S_g
		(Beneficial)	(Non-beneficial)	(Beneficial)	(Non-beneficial)
5000	01	46.036	0.0485	365.1733	618.181
	02	41.527	0.0417	363.9646	595.232
	03	52.650	0.0528	365.6414	627.861
	04	46.588	0.0572	365.2879	621.227
	05	41.421	0.0502	363.9327	592.514
	06	52.009	0.0595	365.7259	631.297
	07	45.286	0.509	365.3106	619.5573
	08	40.376	0.0435	364.0287	**592.2845**
	09	48.962	0.0539	**365.7730**	634.9880

Table 8
Normalized decision matrix table.

Re	Cases	*Nu* (Normalized beneficial)	f (Normalized non-beneficial)	T_{out} (Normalized beneficial)	S_v (Normalized non-beneficial)
5000	01	0.8744	0.8599	0.9984	0.9581
	02	0.7887	1	0.9951	0.9950
	03	1	0.7901	0.9996	0.9433
	04	0.8849	0.7296	0.9987	0.9534
	05	0.7867	0.8309	0.9949	0.9996
	06	0.9878	0.7006	0.9999	0.9382
	07	0.8601	0.8196	0.9987	0.9559
	08	0.7669	0.9589	0.9952	1
	09	0.9299	0.7725	1	0.9327

Table 9
Weighted normalized decision matrix table.

Re	Cases	Weightage For each case	**Nu (Weighted normalized beneficial)**	**f (Weighted normalized** Non-beneficial)	**T_{out} (Weighted normalized Beneficial)**	**S_v (Weighted normalized non-beneficial)**	Performance Score (TPF)
5000	01	0.25	0.2186	0.215	0.2496	0.2395	0.9227
	02		0.1972	0.25	0.2488	0.2488	0.9447
	03		0.2500	0.1975	0.2499	0.2358	0.9333
	04		0.2212	0.1824	0.2497	0.2384	0.8916
	05		0.1967	0.2077	0.2487	0.2499	0.9030
	06		0.2470	0.1751	0.2499	0.2346	0.9066
	07		0.2150	0.2049	0.2497	0.2389	0.9086
	08		0.1917	0.2397	0.2488	0.25	0.9303
	09		0.2325	0.1931	0.2500	0.2332	0.9087

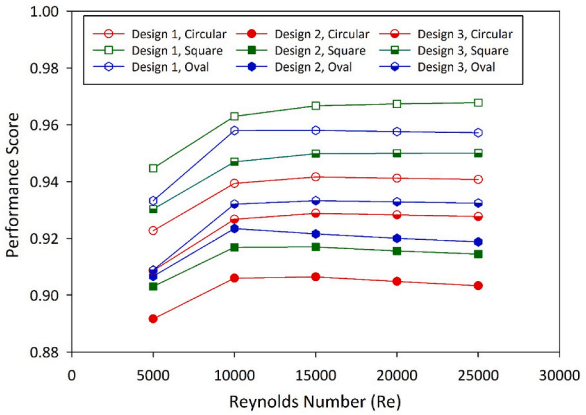

Fig. 15. Comparison of nine cases for TPF using the MCDM approach for Re 5000-25000.

employing six unique ternary hybrid nanofluids (THNF). The prevailing studied parameters were Nusselt number, friction factor, and entropy generation. Multi-criteria decision-making (MCDM) is implemented in order to filter out the best cases. The findings are.

- The velocity streamline plots describe that the fluid mixing is better as existing vorticities are acting, which aids in enhancing heat dissipation for all the cases.
- Heat transfer rate is enhanced with higher fluid velocity. The higher Nusselt number is found for oval cross-section geometries, and the lowest is found for square cross-sectional heat exchangers. The highest Nusselt number is reported for Design 1 with the oval-shaped case.
- The higher outlet temperature is observed for the oval-shaped cross-section, whereas the square-shaped cross-section provides the lower. Design 2, with an oval profile, yields the greatest outlet temperature. Design 1, having a square profile, results in the lowest outlet temperature.

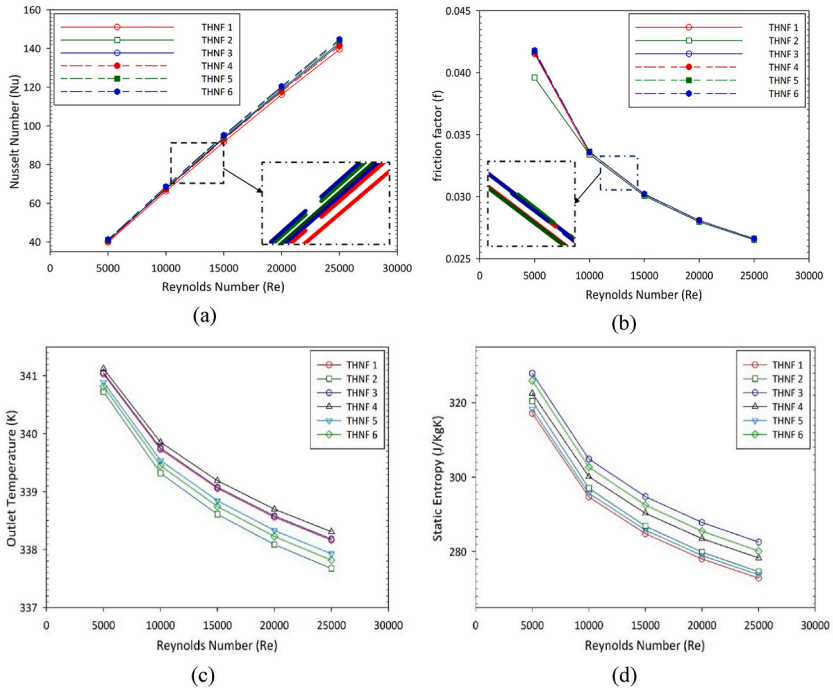

Fig. 16. (a) Nusselt number, (b) Friction factor, (c) Outlet temperature and (d) Static entropy of the six THNF across Re 5000-25000.

- Entropy generation varies with geometrical configurations, and it is found that entropy generation is greater for Design 2 cases. However, lower entropy is found for the Design 1 configuration. The entropy generation is 5 % lower for Design 3 with a square shape configuration at Re = 25000 compared to the case of Design 3 with oval shape geometry at Re = 5000.
- MCDM has been applied with two beneficial and two non-beneficial parameters. Design 1 with square-section performs the best, and Design 2 with circular cross-section, shows poor performance.
- The THNF-6 (Al_2O_3+CNT+Graphene) shows the highest Nusselt number compared to the other five nanofluids. However, the friction factor is lower for THNF-2 (Al_2O_3+CaO+Graphene). On the other hand, the highest outlet temperature is obtained from THNF-4 (Al_2O_3+ZnO+CNT). The lowest static entropy is reported for THNF-1 (Al_2O_3+CaO+ZnO).

CRediT authorship contribution statement

Mostafa Kamal Fahad: Writing – original draft, Validation, Software, Methodology, Investigation, Formal analysis, Data curation, Visualization, Writing – review & editing. **Md. Jahid Hasan:** Writing – review & editing, Writing – original draft, Supervision, Software, Project administration, Methodology, Investigation, Formal analysis, Data curation, Conceptualization. **Nowroze Farhan Ifraj:** Writing – review & editing, Visualization, Software, Investigation, Formal analysis, Data curation, Writing – original draft. **Dipta Chandra Dey:** Software, Investigation, Formal analysis, Visualization, Writing – review & editing.

Declaration of competing interest

The authors declare that they have no known competing financial interests or personal relationships that could have appeared to influence the work reported in this paper.

Funding

The authors affirm that they did not accept any outside funds, grants, or other kinds of assistance for writing this paper.

References

[1] C. Wang, Z. Cui, H. Yu, K. Chen, J. Wang, Intelligent optimization design of shell and helically coiled tube heat exchanger based on genetic algorithm, Int. J. Heat Mass Tran. 159 (2020), https://doi.org/10.1016/j.ijheatmasstransfer.2020.120140.

[2] S. Chamoli, R. Lu, J. Xie, P. Yu, Numerical study on flow structure and heat transfer in a circular tube integrated with novel anchor shaped inserts, Appl. Therm. Eng. 135 (October 2017) (2018) 304–324, https://doi.org/10.1016/j.applthermaleng.2018.02.052.

[3] N.F. Ifraj, M.K. Fahad, S.H. Tahsin, M.R. Haque, M.M. Haque, Numerical investigation of the thermal performance optimization inside a heat exchanger tube using different novel combination of perforations on Y-shaped insert, Int. J. Therm. Sci. 194 (May) (2023) 108583, https://doi.org/10.1016/j.ijthermalsci.2023.108583.

[4] M.J. Hasan, S.F. Ahmed, A.A. Bhuiyan, Geometrical and coil revolution effects on the performance enhancement of a helical heat exchanger using nanofluids, Case Stud. Therm. Eng. 35 (May) (2022) 102106, https://doi.org/10.1016/j.csite.2022.102106.

[5] H. Chen, et al., Thermal/exergy and economic efficiency analysis of circumferentially corrugated helical tube with constant wall temperature, Case Stud. Therm. Eng. 23 (November 2020) (2021) 100803, https://doi.org/10.1016/j.csite.2020.100803.

[6] R.K. Ajeel, K. Sopian, R. Zulkifli, Thermal-hydraulic performance and design parameters in a curved-corrugated channel with L-shaped baffles and nanofluid, J. Energy Storage 34 (October) (2021) 101996, https://doi.org/10.1016/j.est.2020.101996.

[7] R.K. Ajeel, W.S.I.W. Salim, K. Hasnan, Design characteristics of symmetrical semicircle-corrugated channel on heat transfer enhancement with nanofluid, Int. J. Mech. Sci. 151 (November 2018) (2019) 236–250, https://doi.org/10.1016/j.ijmecsci.2018.11.022.

[8] R.K. Ajeel, et al., Turbulent convective heat transfer of silica oxide nanofluid through corrugated channels: an experimental and numerical study, Int. J. Heat Mass Tran. 145 (2019) 118806, https://doi.org/10.1016/j.ijheatmasstransfer.2019.118806.

[9] R.K. Ajeel, W.S.I.W. Salim, K. Hasnan, Experimental and numerical investigations of convection heat transfer in corrugated channels using alumina nanofluid under a turbulent flow regime, Chem. Eng. Res. Des. 148 (2019) 202–217, https://doi.org/10.1016/j.cherd.2019.06.003.

[10] R.K. Ajeel, R. Zulkifli, K. Sopian, S.N. Fayyadh, A. Fazlizan, A. Ibrahim, Numerical investigation of binary hybrid nanofluid in new configurations for curved-corrugated channel by thermal-hydraulic performance method, Powder Technol. 385 (2021) 144–159, https://doi.org/10.1016/j.powtec.2021.02.055.

[11] S.S. Pawar, V.K. Sunnapwar, Experimental and CFD investigation of convective heat transfer in helically coiled tube heat exchanger, Chem. Eng. Res. Des. 92 (11) (2014) 2294–2312, https://doi.org/10.1016/j.cherd.2014.01.016.

[12] R. Kareem, Optimisation of double pipe helical tube heat exchanger and its comparison with straight double tube heat exchanger, J. Inst. Eng. Ser. C 98 (5) (2017) 587–593, https://doi.org/10.1007/s40032-016-0261-x.

[13] J.C. Kurnia, A.P. Sasmito, T. Shamim, A.S. Mujumdar, Numerical investigation of heat transfer and entropy generation of laminar flow in helical tubes with various cross sections, Appl. Therm. Eng. 102 (2016) 849–860, https://doi.org/10.1016/j.applthermaleng.2016.04.037.

[14] H.M. Maghrabie, M. Attalla, A.A.A. Mohsen, Performance of a shell and helically coiled tube heat exchanger with variable inclination angle: experimental study and sensitivity analysis, Int. J. Therm. Sci. 164 (January) (2021) 106869, https://doi.org/10.1016/j.ijthermalsci.2021.106869.

[15] G. Wang, D. Wang, X. Peng, L. Han, S. Xiang, F. Ma, Experimental and numerical study on heat transfer and flow characteristics in the shell side of helically coiled trilobal tube heat exchanger, Appl. Therm. Eng. 149 (2019) 772–787, https://doi.org/10.1016/j.applthermaleng.2018.11.055.

[16] K. Narrein, H.A. Mohammed, Influence of nanofluids and rotation on helically coiled tube heat exchanger performance, Thermochim. Acta 564 (2013) 13–23, https://doi.org/10.1016/j.tca.2013.04.004.

[17] M. Abdelmagied, Thermal performance characteristics of a triple spiral tube heat exchanger, Chem. Eng. Process. - Process Intensif. 149 (2020) 107707, https://doi.org/10.1016/j.cep.2019.107707.

[18] P. Naphon, S. Wiriyasart, R. Prurapark, A. Srichat, Numerical study on the nanofluid flows and temperature behaviors in the spirally coiled tubes with helical ribs, Case Stud. Therm. Eng. 27 (June) (2021) 101204, https://doi.org/10.1016/j.csite.2021.101204.

[19] H. Javadi, S.S. Mousavi Ajarostaghi, M. Pourfallah, M. Zaboli, Performance analysis of helical ground heat exchangers with different configurations, Appl. Therm. Eng. 154 (2019) 24–36, https://doi.org/10.1016/j.applthermaleng.2019.03.021.

[20] S.A. Marzouk, M.M. Abou Al-Sood, E.M.S. El-Said, M.K. El-Fakharany, M.M. Younes, Study of heat transfer and pressure drop for novel configurations of helical tube heat exchanger: a numerical and experimental approach, J. Therm. Anal. Calorim. 148 (13) (2023) 6267–6282, https://doi.org/10.1007/s10973-023-12067-7.

[21] N. Sreenivasalu Reddy, S. Gowreesh Subramanya, K.C. Vishwanath, S. Kanchiraya, V. Satheesha, M. Karthikeyan, Analysis of tube-in-tube copper helical heat exchanger to improve heat transfer, Mater. Today Proc. 39 (2021) 879–887, https://doi.org/10.1016/j.matpr.2020.11.043.

[22] M. Noorbakhsh, M. Pourfallah, S.S.M. Ajarostaghi, M. Zaboli, Numerical evaluation and the effects of geometrical and operational parameters on thermal performance of the shell and double coil tube heat exchanger, Heat Transf. 49 (8) (2020) 4678–4703, https://doi.org/10.1002/htj.21847.

[23] X. Lu, X. Du, M. Zeng, S. Zhang, Q. Wang, Shell-side thermal-hydraulic performances of multilayer spiral-wound heat exchangers under different wall thermal boundary conditions, Appl. Therm. Eng. 70 (2) (2014) 1216–1227, https://doi.org/10.1016/j.applthermaleng.2014.02.053.

[24] K. Pakzad, S.S. Mousavi Ajarostaghi, K. Sedighi, Numerical simulation of solidification process in an ice-on-coil ice storage system with serpentine tubes, SN Appl. Sci. 1 (10) (2019), https://doi.org/10.1007/s42452-019-1316-4.

[25] Y. Cao, H. Ayed, H.S. Dizaji, M. Hashemian, M. Wae-Hayee, Entropic analysis of a double helical tube heat exchanger including circular depressions on both inner and outer tube, Case Stud. Therm. Eng. 26 (May) (2021) 101053, https://doi.org/10.1016/j.csite.2021.101053.

[26] C. Zhang, D. Wang, S. Xiang, Y. Han, X. Peng, Numerical investigation of heat transfer and pressure drop in helically coiled tube with spherical corrugation, Int. J. Heat Mass Tran. 113 (2017) 332–341, https://doi.org/10.1016/j.ijheatmasstransfer.2017.05.108.

[27] M.J. Hasan, A.A. Bhuiyan, Investigation of thermal performance and entropy generation in a helical heat exchanger with multiple rib profiles using Al2O3-water nanofluid, Case Stud. Therm. Eng. 40 (October) (2022), https://doi.org/10.1016/j.csite.2022.102514.

[28] M.R. Salem, K.M. Elshazly, R.Y. Sakr, R.K. Ali, Experimental investigation of coil curvature effect on heat transfer and pressure drop characteristics of shell and coil heat exchanger, J. Therm. Sci. Eng. Appl. 7 (1) (2015) 1–9, https://doi.org/10.1115/1.4028612.

[29] V. Irabatti, Y. Patil, S. Kore, V. Barangule, A. Kothe, Comprehensive review of spiral heat exchanger for diverse applications, Mater. Today Proc. 72 (2023) 1328–1334, https://doi.org/10.1016/j.matpr.2022.09.308.

[30] M. Khoshvaght-Aliabadi, A. Alizadeh, An experimental study of Cu-water nanofluid flow inside serpentine tubes with variable straight-section lengths, Exp. Therm. Fluid Sci. 61 (2015) 1–11, https://doi.org/10.1016/j.expthermflusci.2014.09.014.

[31] A. Mimi Elsaid, M. Ammar, A. Lashin, G.M.R. Assassa, Performance characteristics of shell and helically coiled tube heat exchanger under different tube cross-sections, inclination angles and nanofluids, Case Stud. Therm. Eng. 49 (June) (2023) 103239, https://doi.org/10.1016/j.csite.2023.103239.

[32] M. Mahmoudi, M.R. Tavakoli, M.A. Mirsoleimani, A. Gholami, M.R. Salimpour, Étude expérimentale et numérique du transfert de chaleur par convection forcée et de la chute de pression dans des canalisations enroulées en hélice utilisant le nanofluide TiO2/eau, Int. J. Refrig. 74 (2017) 625–641, https://doi.org/10.1016/j.ijrefrig.2016.11.014.

[33] A.M. Elsaid, E.M.S. El-Said, G.B. Abdelaziz, S.W. Sharshir, H.R. El-Tahan, M.F.A. Raboo, Performance and exergy analysis of different perforated rib designs of triple tubes heat exchanger employing hybrid nanofluids, Int. J. Therm. Sci. 168 (May) (2021) 107006, https://doi.org/10.1016/j.ijthermalsci.2021.107006.

[34] H. Yarmand, et al., Graphene nanoplatelets-silver hybrid nanofluids for enhanced heat transfer, Energy Convers. Manag. 100 (2015) 419–428, https://doi.org/10.1016/j.enconman.2015.05.023.

[35] M. Bouselsal, F. Mebarek-Oudina, N. Biswas, A.A.I. Ismail, Heat transfer enhancement using Al2O3-MWCNT hybrid-nanofluid inside a tube/shell heat exchanger with different tube shapes, Micromachines 14 (5) (2023), https://doi.org/10.3390/mi14051072.

[36] F. Mebarek-Oudina, I. Chabani, H. Vaidya, A.A.I. Ismail, Hybrid-nanofluid magneto-convective flow and porous media contribution to entropy generation, Int. J. Numer. Methods Heat Fluid Flow 34 (2) (2024) 809–836, https://doi.org/10.1108/HFF-06-2023-0326.

[37] A. Ali, F. Mebarek-Oudina, A. Barman, S. Das, A.I. Ismail, Peristaltic transportation of hybrid nano-blood through a ciliated micro-vessel subject to heat source and Lorentz force, J. Therm. Anal. Calorim. 148 (14) (2023) 7059–7083, https://doi.org/10.1007/s10973-023-12217-x.

[38] F. Mebarek-Oudina, et al., Hydromagnetic flow of magnetite–water nanofluid utilizing adapted Buongiorno model, Int. J. Mod. Phys. B 38 (1) (2024) 1–17, https://doi.org/10.1142/S0217979224500036.

[39] H. Adun, D. Kavaz, M. Dagbasi, Review of ternary hybrid nanofluid: Synthesis, stability, thermophysical properties, heat transfer applications, and environmental effects, J. Clean. Prod. 328 (November) (2021) 129525, https://doi.org/10.1016/j.jclepro.2021.129525.

[40] O.A. Alawi, et al., Thermohydraulic performance of thermal system integrated with twisted turbulator inserts using ternary hybrid nanofluids, Nanotechnol. Rev. 12 (1) (2023), https://doi.org/10.1515/ntrev-2022-0504.

[41] M. Arif, P. Kumam, W. Kumam, Z. Mostafa, Heat transfer analysis of radiator using different shaped nanoparticles water-based ternary hybrid nanofluid with applications: a fractional model, Case Stud. Therm. Eng. 31 (August 2021) (2022) 101837, https://doi.org/10.1016/j.csite.2022.101837.

[42] R.R. Sahoo, Thermo-hydraulic characteristics of radiator with various shape nanoparticle-based ternary hybrid nanofluid, Powder Technol. 370 (2020) 19–28, https://doi.org/10.1016/j.powtec.2020.05.013.

[43] I. Ademola, et al., Case Studies in Thermal Engineering Numerical thermal augmentation of ternary nanofluid in a tube with stent , torus-ring and surface-grooved twisted tapes under non-uniform wall temperature, Case Stud. Therm. Eng. 49 (July) (2023) 103308, https://doi.org/10.1016/j.csite.2023.103308.
[44] V. Kumar, R.R. Sahoo, 4 E's (Energy, Exergy, Economic, Environmental) performance analysis of air heat exchanger equipped with various twisted turbulator inserts utilizing ternary hybrid nanofluids, Alexandria Eng. J. 61 (7) (2022) 5033–5050, https://doi.org/10.1016/j.aej.2021.09.037.
[45] H. Berrehal, S. Dinarvand, I. Khan, Mass-based hybrid nanofluid model for entropy generation analysis of flow upon a convectively-warmed moving wedge, Chinese J. Phys. 77 (2022) 2603–2616, https://doi.org/10.1016/j.cjph.2022.04.017.
[46] G. Dharmaiah, S. Dinarvand, J.L. Rama Prasad, S. Noeiaghdam, M. Abdollahzadeh, Non-homogeneous two-component buongiorno model for nanofluid flow toward Howarth's wavy cylinder with activation energy, Results Eng 17 (2023) 100879, https://doi.org/10.1016/j.rineng.2023.100879.
[47] M.A. Radwan, M.R. Salem, H.A. Refaey, M.A. Moawed, Experimental study on convective heat transfer and pressure drop of water flow inside conically coiled tube-in-tube heat exchanger 1 (39) (2019) 86–93.
[48] B.A. Gizzetdinovna, Engineering Calculation and Experimental Study of a Cone-Shaped Coil Heat Exchanger, vol. 10, 2020, pp. 163–173.
[49] S. Rashidi, N. Bakhshi, R. Rafee, Progress and challenges of helical-shaped geothermal heat exchangers, Environ. Sci. Pollut. Res. 28 (23) (2021) 28965–28992, https://doi.org/10.1007/s11356-021-13766-0.
[50] U. Manual, Ansys FLUENT 12.0, Theory Guid 67 (2009).
[51] Adnan, W. Ashraf, Thermal efficiency in hybrid (Al2O3-CuO/H2O) and ternary hybrid nanofluids (Al2O3-CuO-Cu/H2O) by considering the novel effects of imposed magnetic field and convective heat condition, Waves Random Complex Media (2022), https://doi.org/10.1080/17455030.2022.2092233.
[52] N.H. Abu-Hamdeh, E.M. Salilih, Numerical modelling of a parallel flow heat exchanger with two-phase heat transfer process, Int. Commun. Heat Mass Tran. 120 (2021) 105005, https://doi.org/10.1016/j.icheatmasstransfer.2020.105005.
[53] R.H. Monfared, M. Niknejadi, D. Toghraie, P. Barnoon, Numerical investigation of swirling flow and heat transfer of a nanofluid in a tube with helical ribs using a two-phase model, J. Therm. Anal. Calorim. 147 (4) (2022) 3403–3416, https://doi.org/10.1007/s10973-021-10661-1.
[54] M. Sahu, J. Sarkar, Steady-state energetic and exergetic performances of single-phase natural circulation loop with hybrid nanofluids, J. Heat Tran. 141 (8) (2019) 1–46, https://doi.org/10.1115/1.4043819.
[55] S. Dinarvand, H. Berrehal, H. Tamim, G. Sowmya, S. Noeiaghdam, M. Abdollahzadeh, Squeezing flow of aqueous CNTs-Fe3O4 hybrid nanofluid through mass-based approach: effect of heat source/sink, nanoparticle shape, and an oblique magnetic field, Results Eng 17 (February) (2023) 100976, https://doi.org/10.1016/j.rineng.2023.100976.
[56] S. Dinarvand, H. Berrehal, I. Pop, A.J. Chamkha, Blood-based hybrid nanofluid flow through converging/diverging channel with multiple slips effect: a development of Jeffery-Hamel problem, Int. J. Numer. Methods Heat Fluid Flow 33 (3) (2023) 1144–1160, https://doi.org/10.1108/HFF-08-2022-0489.
[57] S. Dinarvand, M. Behrouz, S. Ahmadi, P. Ghasemi, S. Noeiaghdam, U. Fernandez-Gamiz, Mixed convection of thermomicropolar AgNPs-GrNPs nanofluid: an application of mass-based hybrid nanofluid model, Case Stud. Therm. Eng. 49 (February) (2023) 103224, https://doi.org/10.1016/j.csite.2023.103224.
[58] M.K. Fahad, N.F. Ifraj, S.H. Tahsin, M.J. Hasan, Numerical investigation of the hydrothermal performance of novel vortex generators in a rectangular channel by employing inclination and rotational angles, Int. J. Thermofluids 20 (2023) 100500, https://doi.org/10.1016/j.ijft.2023.100500.
[59] R.L. Manlapaz, S.W. Churchill, Fully developed laminar flow in a helically coiled tube of finite pitch, Chem. Eng. Commun. 7 (1–3) (1980) 57–78, https://doi.org/10.1080/00986448008912549.